ITATION PAGE

AD-A244 572

| T DATE | 3. REPORT TYPE AND DATES COVERED |
| June 1991 | Preprint |

4. TITLE AND SUBTITLE
A Quantitative Study of Unsteady Compressible Flow on an Oscillating Airfoil

5. FUNDING NUMBERS

ARO MIPR 114-91

6. AUTHOR(S)
L. W. Carr, M. S. Chandrasekhara and N. J. Brock

7. PERFORMING ORGANIZATION NAME(S) AND ADDRESS(ES)
Naval Postgraudate School
Dept. of Aeronautics & Astronautics
Monterey, CA 93943

8. PERFORMING ORGANIZATION REPORT NUMBER

--

9. SPONSORING/MONITORING AGENCY NAME(S) AND ADDRESS(ES)
U. S. Army Research Office
P. O. Box 12211
Research Triangle Park, NC 27709-2211

10. SPONSORING/MONITORING AGENCY REPORT NUMBER

ARO 27894.7-EG

11. SUPPLEMENTARY NOTES AIAA Paper No. 91-1683
The view, opinions and/or findings contained in this report are those of the author(s) and should not be construed as an official Department of the Army position, policy, or decision, unless so designated by other documentation.

12a. DISTRIBUTION/AVAILABILITY STATEMENT

Approved for public release; distribution unlimited.

12b. DISTRIBUTION CODE

13. ABSTRACT (Maximum 200 words)

Detailed interferometric measurements of the flow near the leading edge of an oscillating airfoil offer the first detailed experimental quantification of the locally compressible flow field that surrounds an oscillating airfoil at moderate subsonic Mach numbers. Interferograms obtained by a specially adapted real-time point-eiffraction interferometry technique have revealed significant characteristics of this complex, and very rapidly varying, locally supersonic flow. Instantaneous pressure distributions determined from these interferograms document the effect of unsteadiness on the leading-edge flow environment.

92-00953

DTIC
JAN 21 1992

92 1

14. SUBJECT TERMS
Dynamic Stall, Quantitative real-time interferometry, Compressibility effects, Unsteady flow measurement

15. NUMBER OF PAGES
16

16. PRICE CODE

| **17. SECURITY CLASSIFICATION OF REPORT** | **18. SECURITY CLASSIFICATION OF THIS PAGE** | **19. SECURITY CLASSIFICATION OF ABSTRACT** | **20. LIMITATION OF ABSTRACT** |
| UNCLASSIFIED | UNCLASSIFIED | UNCLASSIFIED | UL |

AIAA-91-1683

A Quantitative Study of Unsteady Compressible Flow on an Oscillating Airfoil

L. W. Carr , U.S.Army AVSCOM, and
NASA-Ames Research Center, Moffett Field, CA;
M. S. Chandrasekhara, Naval Postgraduate School,
Monterey, CA;
N. J. Brock, Aerometrics, Sunnyvale, CA.

AIAA 22nd Fluid Dynamics, Plasma Dynamics & Lasers Conference
June 24-26, 1991 / Honolulu, Hawaii

A QUANTITATIVE STUDY OF UNSTEADY COMPRESSIBLE FLOW ON AN OSCILLATING AIRFOIL

L.W. Carr[1]
Aeroflightdynamics Directorate, U.S.Army AVSCOM
and Fluid Dynamics Research Branch
NASA Ames Research Center, Moffett Field, CA 94035

M.S. Chandrasekhara[2]
Navy-NASA Joint Institute of Aeronautics
Department of Aeronautics and Astronautics
Naval Postgraduate School, Monterey, CA 93943

N.J. Brock[3]
Aerometrics, Sunnyvale, CA 94086

ABSTRACT

Detailed interferometric measurements of the flow near the leading edge of an oscillating airfoil offer the first detailed experimental quantification of the locally compressible flow field that surrounds an oscillating airfoil at moderate subsonic Mach numbers. Interferograms obtained zby a specially adapted real-time point-diffraction interferometry technique have revealed significant characteristics of this complex, and very rapidly varying, locally supersonic flow. Instantaneous pressure distributions determined from these interferograms document the effect of unsteadiness on the leading-edge flow environment.

Nomenclature

C_p	pressure coefficient
c	airfoil chord
f	frequency of oscillation, Hz
k	reduced frequency $= \frac{\pi f c}{U_\infty}$
L	test section span
M_∞	free stream Mach number
n	refractive index
n_r	refractive index at reference conditions
n_0	refractive index at atmospheric conditions
n	distance along airfoil surface
U_∞	free stream velocity
x	chordwise distance
α	angle of attack
$\overline{\Delta PL}$	average path length difference
ϵ	fringe number

1 *Group Leader, Unsteady Viscous Flows; Member AIAA; Mailing Address: M.S. 260-1, NASA Ames Research Center, Moffett Field, CA 94035*

2 *Assistant Director and Adjunct Research Professor; Assoc. Fellow AIAA*

3 *Research Scientist*

λ_0	wavelength of the laser
ρ	density
ρ_0	density at atmospheric conditions
ρ_r	density at reference conditions
ϕ	phase angle of oscillation
ω	circular frequency, radians/sec

1. INTRODUCTION

Quantification of the complex unsteady flow field associated with dynamic stall continues to be of significant importance. The present inability to control and/or modify the dynamic stall phenomenon has limited the speed and agility of helicopters, and has seriously restricted the use of unsteady lift for improvement of aircraft agility and maneuverability. Many studies of this aerodynamic phenomenon have been performed; see Carr[1] for summary. Recent studies using the facility described in the present paper have shown that compressiblity effects can and do play a significant role in the development of the unsteady flow field on rapidly pitching airfoils[2,3]. However, truly quantitative, simultaneous documentation of the compressible flow field on and away from the surface of the airfoil has not been available up to the present. Surface measurements have been made in the past[4,5], but knowledge of the flow behavior away from the surface is also necessary before control and/or modification of the stall process can be implemented. The work presented in this paper supplies some of this critical information.

2. FACILITY AND INSTRUMENTATION

The present study was performed in the Compressible Dynamic Stall Facility(CDSF) at the NASA Ames Research Center Fluid Mechanics Laboratory. The CDSF is specifically designed for study of dynamic stall over a range of Mach numbers, using non-intrusive optical flow diagnostic techniques. It is operated as a part of the in-draft tunnel complex at the FML(for details see Carr and Chandrasekhara, Reference 6). The CDSF is unique in that the airfoil is supported between two 2.54 cm thick optical quality glass windows by pins that are smaller than the local airfoil thickness. Thus, the entire flow field includ-

ing the airfoil surface can be viewed unobstructed by any support mechanism(Figure 1). This permits the study of the flow at the surface near the leading edge, where the dynamic stall vortex forms, as well as the flow field away from the airfoil. Details of the research findings from the earlier work in this facility can be found in References 2, 3 and 6. The present tests were performed for $\alpha = 10^o$ - $10^o sin\omega t$, $0.28 \leq M_\infty \leq 0.47$, and $0.0 \leq k \leq 0.10$.

3. FLOW VISUALIZATION

3.1 Point Diffraction Interferom·try Technique

Point diffraction interferometry(PDI) is a technique which permits recording of real-time interferograms of a flow[7-10]. The PDI technique utilizes the ability of a point discontinuity(in the form of a pinhole or an opaque spot), located at the image of a point source(Fourier transform plane), to diffract a portion of the incident light into a spherical reference wave front. Light passing through the phase object under test is focused onto a sheet of partially transmitting material containing the pinhole(see Figure 2). A portion of this light is diffracted by the pinhole creating a reference wavefront. The resulting reference wavefront then interferes with the undiffracted light that passes around the pinhole. The interference fringes which are produced by this method provide a contour of optical path difference caused by density variations in the flow field. Since the mathematical derivations associated with PDI are well documented in the referenced papers[7-9], the present paper will only address the physical implementation.

3.2 Implementation

In the present application, the primary optics of an existing schlieren system are used, with a pulsed Nd-YAG laser replacing the conventional spark as the light source, and the above mentioned point diffractor replacing the usual knife edge. Figure 3 shows a schematic of the arrangement. Laser light is expanded to fill a portion of the first schlieren mirror, where it reflects through the test section and finally is refocused onto the diffracting plate by the second schlieren mirror. A camera placed at the image plane of the flow field records the interference pattern.

Diffracting spots and pinholes were made by placing a photographic emulsion precisely at the focus of the second schlieren mirror. With no flow in the test section, laser energy was increased until a spot was charred on the emulsion, or until a pinhole was burned through the emulsion. Although some of the earlier data was obtained with diffracting spots, pinholes were used in the present experiment since the interferograms produced using pinholes were brighter and of superior quality. Once the pinhole was made, it was left in place, and the laser energy decreased to a level that adequately exposed the camera film without destroying the pinhole.

The photographic plate(Agfa 8E75) used to make the diffracting pinhole was processed with a weak developer and then exposed uniformly with light in order to make the emulsion darker(plates with emulsions darkened to optical densities of approximately one were used for the flow situations encountered in this test); no other processing was required. The increased absorption is necessary to attenuate the light passing around the pinhole(object wave) to a level equal in intensity to the light which diffracts from the pinhole (reference wave), thereby maximizing fringe contrast. The optical density necessary depends on how much the light is disturbed as it passes through the test section. An increase in disturbance(caused by stronger density gradients such as those that appear at high angle of attack) results in an increase in the diameter of the focused beam at the pinhole, thereby decreasing the light diffracting through the pinhole, thus requiring a higher optical density for the PDI plate for optimum fringe contrast.

An alternate method of matching the beam intensities was used for certain conditions. This method used carefully controlled laser energy to burn varying sizes of pinholes. Since a wide range of density gradients were encountered in the flow fields of interest, frequent variation of either emulsion density or pinhole was required. This latter method of matching beam intensities required the least effort, and was used for most of the interferograms presented.

4. FLOW CHARACTERISTICS

4.1 General Flow Characteristics

The interferogram presented in Figure 4 shows in detail the developing compressible flow field around the leading edge of the pitching airfoil just prior to the initiation of dynamic stall. This figure presents the flow at $\alpha = 10.0^o$ for $M_\infty = 0.33$, and k = 0.075, and shows several characteristics of the unsteady flow field that are of significant interest. First, the stagnation point on the lower surface is easily discernable, at the center of the smallest closed contour of constant density; since the flow speed increases from the stagnation point in both directions on the lower surface of the airfoil, it is clear that the stagnation point is centered in this fringe. It should also be noted that this stagnation point quantifies the density field for the complete interferogram, since the stagnation pressure of the surrounding flow is attained at the stagnation point on the airfoil. This allows quantification of the fringe-related Mach contours for the complete flow field around the airfoil.

The flow accelerates as it progresses around the leading edge, as can be seen in the closely spaced fringes emanating from the leading edge region. A small region where no image is present can be observed here at the leading edge; this region is dark due to the fact that much of the light has been so severely deflected by the flow gradients that it is not able to reach the photographic plate. thus leaving a dark region on the film. Considerable effort was expended during the alignment phase to minimize this dark region; in addition, during analysis, the image in this region was further improved using a digital enhancement technique described below. As the flow continues to move around the airfoil, it continues to accel-

erate, until the surface curvature is reduced, where a plateau appears in the density contours. This region is of significant interest, since surface pressure measurements performed in earlier experiments[4] suggest locally supersonic flow in this region based on isentropic expansion to the surface pressure measured by that experiment. However, the constant-density contours obtained in the present experiment show that for the present experimental conditions, this supersonic region, if present at all, is constrained to a very thin region near the surface of the airfoil. For example, at $M_\infty = 0.3$, the highest Mach number observed in the contour lines of the present experiment only reach $M_{local} = 0.84$(compared to the $M_{local} = 1.3$ inferred from surface pressure measurements[4]).

It is also of interest that this region shows very little longitudinal gradient, and in fact shows the constant-density contours to be almost parallel to the surface of the airfoil in this region. Further down the airfoil, these contours abruptly turn toward the surface. The shape of the fringe contours in this region suggest the presence of a laminar separation bubble. The conditions of the present experiment(NACA 0012 airfoil, Re = 600,000) are appropriate for a laminar bubble to appear near the leading edge of the airfoil. The formation of the laminar separation bubble was also confirmed by the laser doppler velocimetry(LDV) studies performed in the CDSF[11,12] for $M_\infty = 0.3$, k = 0.05. The angles of attack at which the bubble forms $\alpha = 6^o$, and opens $\alpha = 14^o$ are nearly the same using both LDV and PDI. The contour lines outside this region curve more gradually toward the surface, and can be seen to define the boundary layer over the remaining portion of the airfoil surface.

Figure 5 presents the flow field for $\alpha = 13.6^o$. In this figure, the dynamic stall vortex has formed, and the density field can be seen to be dramatically altered. The development of the flow near the surface in this case is of considerable interest. The most significant change in the character of the flow appears on the upper surface near the leading edge. There is now a clearly defined shear layer leaving the leading edge; this shear layer shows very strong gradients, as evidenced by the bending of the light sufficiently to produce an opaque image. Also, the flow field normally associated with the dynamic stall vortex shows a strong longitudinal gradient as depicted by the vertical density contours appearing along the upper surface near 25% chord. This figure presents a quantitative image of the Mach number environment of the airfoil at this point in the oscillation, and can be used directly to evaluate the accuracy of computational models of the dynamic stall process.

4.2 Analysis of Stall Onset Process

Detailed analysis of the interferograms obtained in the present experiment show that the flow only attains a local Mach number of .83 at k=.05, M_∞ = 0.30, $\alpha = 10^o - 10^o sin\omega t$, even though in earlier experiments[4] surface pressures suggested local Mach numbers as high as 1.3. The two experiments are similar in many respects: both were run at $M_\infty = 0.30$; both performed for $\alpha = 10^o - 10^o sin\omega t$; both tests were on the NACA0012 airfoil. However, the present

tests were performed at a chord Reynolds number of 600,000, while the previous tests were performed at Re = 4×10^6. A review of the data from the earlier experiments[4] shows that the NACA0012 airfoil at M=.30, k=0.05, $\alpha = 10^o - 10^o sin\omega t$ reached a local Mach number of 1.22 at an $\alpha = 13.9^o$, at which point the leading edge suction peak was lost, and the dynamic stall process began. The present experiments for the same test conditions show dynamic stall to begin at $\alpha = 12.0^o$.

A laminar separation bubble was observed in the earlier tests[4], where it appeared as an abrupt change in skin friction magnitude and frequency content. However, it was only of secondary importance in its influence on the pressure distributions and appeared as a small, localized "wiggle" in the pressure traces. The effect of the bubble was determined to be secondary, since the leading edge suction remained high well after the laminar separation bubble was detected, and the loss of suction peak appeared at the leading edge, well ahead of the laminar bubble,. As noted above, a laminar separation bubble has also been identified in the present set of experiments. However, in the present case, the bubble remains a significant factor in the dynamic stall development - in fact, the bubble behavior seems to be the first indicator that the dynamic stall process has begun. The character of the laminar separation bubble changes significantly as the dynamic stall process develops. The bubble appears at at angles above $\alpha = 6^o$ across a wide range of frequencies and Mach numbers. Although its appearance is delayed by oscillation at $\alpha = 8^o$(see following section), it is essentially unaffected by frequency or Mach number at any higher angle of attack. The constant-density fringes emanating from the leading edge curve flatten significantly in this region, indicating an alleviation of the local pressure gradient. It is possible that since this bubble is larger than in the previous test[4], its influence on the displacement thickness of the boundary layer is the source of the drop in maximum Mach number that has been observed throughout this set of experiments.

The bubble remains intact up to the dynamic stall angle. Figure 6 presents an interferogram illustrating the typical bubble geometry, for $M_\infty = 0.33$, k = 0.075, and $\alpha = 9^o$(below the static stall angle). This figure shows the fringes near the airfoil are parallel to the surface, followed by a sharp curving toward the surface at the end of the bubble. The pressure distribution determined from this interferogram is shown in Figure 7. The maximum suction seen in this figure is approximately -2.2, and a plateau appears following the suction peak, extending from $.015 \leq x/c \leq 0.05$(the length of the bubble). The maximum Cp observed in this figure is significantly less that that suggested by surface-mounted instantaneous pressure transducers due to lack of detail in this region of the photograph; further research will focus on this region in order to quantify the details of the suction peak. A region of adverse pressure gradient develops for $0.05 \leq x/c \leq 0.08$, in which the dCp/dx values reach a high of 250 while the Cp increases to approx -1.5. The pressure then gradually increases over the rest of the airfoil, in a pattern similar to that of steady flow. For comparison, an interferogram obtained at $\alpha = 12.4^o$ is presented in Figure

3

8. Here, the fringe pattern is similar near the leading edge, and the beginning of the bubble, but the downstream edge of the bubble now has fringes extending downstream, parallel to the surface, in contrast to the sharp turning toward the surface seen in Figure 6. In fact, the first indication of breakdown of the flow leading to dynamic stall appears as this change of the fringe contours at the downstream end of the bubble, suggesting a failure of the turbulent flow to reattach. Finally, Figure 9, at $\alpha = 13.07°$, shows the beginning of the dynamic stall vortex, which develops from the extended bubble shown in Figure 8. The fringes near the surface downstream of the bubble have now turned sharply toward the surface. Since each fringe indicates a specific density, this image shows that there is now a region of low density, and therefore pressure, extending along the airfoils surface. This also affects the flow away from the surface, as can be seen in the outer fringes which also curve around this low pressure region. This pattern of opening of the laminar separation bubble was detected throughout the frequency and Mach number range explored to date, and suggests that the dynamic stall process in the present experiment is either caused by a breakdown of the laminar separation bubble, or by events occurring within the bubble which have yet to be documented. This is of significant interest, since it re-emphasizes that dynamic stall can be caused by a wide range of fluid physics while resulting in very similar global flow behavior. Future tests in the present program will investigate various types of leading-edge boundary layer transition generators, so that the CDSF airfoil can fully reproduce the various types of leading- and trailing-edge dynamic stall conditions observed in full scale tests.

4.3 Influence of Reduced Frequency and Mach Number

REDUCED FREQUENCY: The effect of reduced frequency on the flow developing on the airfoil can be seen in Figure 10. In this figure, the influence of unsteadiness is shown at each of four angles of attack. The top row of photographs shows the effect of frequency on the flow at $\alpha = 8°$. The presence of the laminar separation bubble can be seen at k = 0.0. At this angle of attack, the bubble is suppressed by oscillation; the flow at k = 0.075 and 0.10 do not show the bubble - the contours are similar to those at lower angle of attack(not shown). At $\alpha = 10°$(second row of photographs) the bubble is present throughout the frequency range. At $\alpha = 12°$(third row of photographs), the first indication that oscillation delays stall is observed: the steady flow is stalled, but even low level oscillation(k = 0.025) suppressed separation and re-establishes fully attached flow. At $\alpha = 14°$, the influence is even more clearly discernable: as the frequency increases to k = 0.05 and higher, the stall is suppressed, and a dynamic stall vortex appears. The development of this vortex is delayed as the frequency is increased. Thus, as the frequency reaches k = 0.10, the dynamic stall process is just beginning at an angle two degrees higher than the angle at which the airfoil was completely stalled in steady flow.

MACH NUMBER: The effect of Mach number at k = 0 05 can be seen in Figure 11. At $\alpha = 6°$(first row of photographs), the flow varies smoothly from the stagnation point to the trailing edge(out of the view of the photograph). As the Mach number is increased, a progressive increase in the fringe count is apparent, as can be expected, due to the greater density variations that occur at the higher Mach numbers. At $\alpha = 8°$ (second set of photographs), the presence of the laminar separation bubble is observed. This bubble is not measurably altered as the Mach number is increased, except for the increase in fringe density reflecting the increase in Mach number. At $\alpha = 10°$(third row), some very interesting flow physics can be seen in the laminar separation bubble. As the Mach number increases to $M_\infty = 0.42$, vertical lines appear in the bubble. These vertical lines appear even more clearly at $M_\infty = 0.47$, where the fringes are seen to bend discontinuously as they pass through the vertical lines. The local Mach number obtained by fringe counting was found to be 1.0 - 1.1; thus, the local flow is slightly supersonic. The multiple shock waves seen are a feature of the transonic flow over mildly curving surfaces; this condition of multiple shocks have been observed in other experiments[13,14]. It is very interesting that the current study shows the phenomenon to be present even in unsteady flows, where the events occur at different angles of attack depending on the reduced frequency.

At $\alpha = 12°$(fourth row), the influence of compressibility on the dynamic stall process is quite evident. The flow on the airfoil at $M_\infty = 0.28$ is clearly attached, as is the flow at $M_\infty = 0.30$. However, at $M_\infty = 0.33$, the dynamic stall process has begun, and at $M_\infty = 0.38$ the dynamic stall vortex is evident. At $M_\infty = 0.42$, the vortex is already past x/c = .25, and at $M_\infty = 0.47$, the vortex is already out of the field of view. These photographs graphically show that the dynamic stall inception angle is a direct function of the Mach number.

5. QUANTITATIVE ANALYSIS OF THE UNSTEADY FLOW FIELD

5.1. Mach Contours

The interferograms presented in this study offer quantitative information concerning the Mach contours of the flow under investigation.

For a standard interferometer, the path length difference $\overline{\Delta PL}$ due to density (or phase) changes can be related to the fringe number ϵ as,

$$\epsilon = \frac{\overline{\Delta PL}}{\lambda_0} = \frac{1}{\lambda_0} \int (n - n_{ref}) dz$$

where n is the refractive index in the signal beam, n_{ref} is that in the reference beam and λ_0 is the wave length of the light used.

For a two-dimensional flow, the above equation can be simplified to,

$$\epsilon = (n - n_{ref}) \frac{L}{\lambda_0}$$

where L is the test section span. If ϵ is an integer, then the fringe is bright and if it is a half integer, the

fringe is dark. Using the Gladstone - Dale equation and the perfect gas equation, this equation can be reduced to (See Goldstein, Reference 15)

$$\rho - \rho_{ref} = (\frac{\lambda_0}{n_0 - 1})(\frac{\epsilon \rho}{L}) = A\epsilon$$

Since $\lambda_0 = 532$ nm, L = 25cm, $(n_0 - 1) = 2.733$ x 10^{-4} (from Goldstein), and $\rho_0 = 1.21 kg/m^3$, the constant A can be determined. For the specific case of the present experiments,

$$\rho - \rho_0 = 0.009421\epsilon$$

or

$$\frac{\rho}{\rho_0} = \frac{\rho_r}{\rho_0} + \frac{A\epsilon}{\rho_0}$$

Since $\frac{\rho_r}{\rho_0}$ is a function of the free stream Mach number only, $\frac{\rho}{\rho_0}$ can be determined by knowing the fringe number. Note that in this method, a positive fringe number represents deceleration and vice versa.

5.2 Digitization of Interferograms

In order to make full use of the quantification that interferometry offers, the photographs containing the interferograms were digitally processed, and the leading edge region was greatly enlarged. Three registration markers were placed on one of the rotating tunnel windows which support the airfoil so that a proper orientation and scaling of the fringe patterns could be accomplished(Figure 12). The two triangles below the airfoils are arranged so that the distance between the vertical faces is exactly 20% chord; the horizontal surfaces of these triangles are placed so that a line connecting these surfaces is parallel to the airfoil chord, and 10% below the center line of the airfoil. The triangle above the airfoil is placed so that its lower surface is 20% chord from the top surface of the triangle located below the airfoil. A line connecting the vertical surfaces of these two triangles will be perpendicular to the chord at the 25% chord location. Each interferogram was digitally scanned, and scaled to a selected size by use of these registration markers. A grid was superimposed on the digitized image, and the grid block containing the leading edge region was selected for further enlargement. This image was then processed using an adaptive contrast-enhancement procedure specially developed for this purpose. This procedure subdivided the region before applying the enhancement, and then locally optimized the contrast. The locally optimized contrast in each subregion was then smoothly matched to the adjoining regions, resulting in a greatly improved interferogram for digital fringe mapping(Figure 13). This image shows a clear delineation of the airfoil surface. This clarity was obtained by using a photograph of the airfoil taken under no-flow conditions, with the PDI plate removed. This no-flow airfoil image was then digitized, scaled, and superimposed on the digitized image of the interferogram, and the combined digital image was then used for further analysis.

The combined image was then mapped using a specially-designed, screen-oriented digitizing program which interactively permitted tracing of the various fringes by movement of the cursor via a computer "mouse". Samples of the resultant fringe contour maps can be seen in Figures 14 and 15.

5.3 Instantaneous Pressure Distributions

Each fringe in an interferogram is a line of constant density, and by use the procedure outlined in Section 5.1, denotes a constant Mach number. Therefore, the fringe maps described above can be used to quantify the effect of unsteadiness on the local pressure distributions of the oscillating airfoil studied in the present experiments. Figure 16 presents pressure distributions near the leading edge of the airfoil for four steady angles of attack at $M_\infty = 0.33$. These plots are obtained by mapping the x-location of the intersection of each fringe with the airfoil surface. The fringe numbers are then converted to Cp, and the pressure distributions calculated. In each case shown, the distributions are mapped up to the point where the last fringe intersects the surface before the laminar separation bubble occurs, and thus show the pressure distribution associated with the laminar bubble formation(except for $\alpha = 4°$, where the bubble was not present).

Figure 17 presents the pressure distributions at k=0.05 and k=0.10 at $\alpha = 8°$. The pressure distributions for steady flow at $\alpha = 6°$ and $8°$ are included for comparison. The curves for k = 0.05, and 0.10 are flatter and thus show progressively lower gradients. The pressure distribution for k = 0.10, at $\alpha = 8°$ is virtually identical to the distribution for k = 0.0, $\alpha = 6°$, showing that unsteadiness has indeed reduced the instantaneous local pressure gradients. This experimental evidence of the lessening of local adverse pressure gradient is the first data to show this detail of the developing pressure gradients, since the cost and complexity of installation of instantaneous pressure transducers in sufficient number to show this detail has precluded such endeavors in the past.

Figure 18 presents the maximum(suction) Cp values as a function of the angle of attack at $M_\infty = 0.33$, k= 0.075. The maximum Cp was determined by counting the fringes through the stall vortex and tracing them back to the leading edge; in the attached flow near the leading edge, any particular fringe can be assigned a Cp value using isentropic flow relations. This plot shows that suction steadily develops over the airfoil as the angle of attack increases. At $\alpha = 12.5°$, the Cp has reached a value = -4.7, and remains at this level till $\alpha = 13.2°$, where it starts decreasing. It is believed that the dynamic stall process begins at $\alpha = 12.5°$ in this case; during the vortex formation the suction peak remains constant. However, once the vortex begins to convect, the suction peak drops. It is interesting that even though the suction peak drops, there is a substantial suction present over the airfoil as the vortex grows, and the increased extent of the low pressure region enables generation of higher lift until the vorticity leaves the airfoil.

LIMIT ON Cp MIN: Also plotted in Figure 18 are the minimum Cp values for $M_\infty = 0.3$ at k=0.05, 0.075, and 0.10, when they are first observed(i.e. before the vortex could be detected in the interfero-

grams). It is seen that $Cp_{min} = -4.96$ for all three cases at $M_\infty = 0.3$. The most noteworthy difference is that as the reduced frequency increases, the angle of attack at which the peak suction is encountered and the stall process begins also increases. For example, $\alpha_{stall} = 12.13°$, $12.5°$, and $13.14°$ for k = 0.05, 0.075, and 0.10 respectively. These results clearly suggest that, at a given Mach number, stall develops once the Cp value reaches a unique value, independent of reduced frequency. Since the value is reached at progressively higher angles with increasing frequency, oscillating an airfoil at higher frequencies delays the stall to higher angles. As has been shown in Figure 17, the pressure gradients are also reduced by oscillation, resulting in lowering of the equivalent instantaneous angle of attack. Thus, at least part of the delay of stall can be viewed as a modification of the inviscid flow imposed on the boundary layer. The effect of compressibility on this flow development is apparent in that as the Mach number is increased, the Cp_{min} value decreases, as can be seen in the figure for $M_\infty = 0.4$, k = 0.05, where a value of -3.9 is attained at $\alpha = 11.2°$.

6. CONCLUDING REMARKS

Point diffraction interferometry has permitted detailed study of the complex unsteady flow near the leading edge of an oscillating airfoil, and quantitative flow information has been obtained both on the surface and in the surrounding flow field for a range of frequencies and Mach numbers. A laminar separation bubble is observed in most of the higher angle conditions, although the occurrence of the bubble can be delayed by unsteadiness. Locally supersonic flow was observed near the leading edge, but the region of supersonic flow is quite small. Digitization of the interferograms has permitted detailed mapping of the instantaneous pressure distribution near the leading edge, and has shown that unsteadiness significantly relieves the pressure gradients that occur in this region.

ACKNOWLEDGEMENTS

8. REFERENCES

1. Carr, L.W., "Progress in Analysis and Prediction of Dynamic Stall", J of Aircraft, Vol. 25, No. 1, 1988, p 6-17.

2. Chandrasekhara, M.S. and Carr, L.W., "Flow Visualization Studies of the Mach Number Effects on Dynamic Stall of an Oscillating Airfoil", J of Aircraft, Vol 27, No 6, pp 516-522, June 1990.

3. Carr, L.W., Platzer, M.F., Chandrasekhara, M.S., and Ekaterinaris, J., "Experimental and Computational Studies of Dynamic Stall", Numerical and Physical Aspects of Aerodynamic Flows IV, T. Cebeci, editor, Springer-Verlag, publisher, pg 239-258, 1990.

4. McCroskey, W.J., McAlister, K.W., Carr, L.W., Pucci, S.L., Lambert, O., and Indergand, R.F., "Dynamic Stall on Advanced Airfoil Sections", J Am. Helicopter Soc, pp 40-50, July 1981.

5. Lorber, P.F., and Carta, F. O., "Airfoil Dynamic Stall at Constant Pitch Rate and High Reynolds Number", J of Aircraft, Vol. 25, No. 6, pp 548-556, June 1988.

6. Carr, L.W., and Chadrasekhara, M.S., "Design and Development of a Compressible Dynamic Stall Facility", AIAA 89-0647, 27th Aerospace Sciences Meeting, January 9-12, 1989(accepted for publication in the J of Aircraft).

7. Smartt, R.N., "Point-Diffraction Interferometry as a Diagnostic Tool for Alignment", SPIE Volume 483, Optical Alignment II, 1984.

8. Bachalo, W.D., and Houser, M.J., "Evaluation and Application of a New Interferometric Technique for Compressible Flow Research", NASA CR-177467, Oct. 1988.

9. Anderson, R.C., and Milton, J.E., "A Large aperture Inexpensive Interferometer for Routine Flow Measurements", Proc of International Conference on Instrumentation in Aerospace Simulation Facilities, pp 394-399, Goettinger, FRG, September 18-21, 1989.

10. Carr, L.W., Chandrasekhara, M.S., Brock, N.J., and Ahmed, S., "A Study of Dynamic Stall Using Real-Time Interferometry", AIAA 91-0007, 29th Aerospace Sciences Meeting, Reno, NV, January 7-10, 1991.

11. Chandrasekhara, M.S., and Van Dyken, R., "Oscillating Airfoil Velocity Field During Large Amplitude Dynamic Stall", Proceedings of the 8th Symposium on Turbulent Shear Flow, Munich, Germany, September 9-12, 1991.

12. Chandrasekhara, M.S., and Ahmed, S., "Laser Velocimetry Measurements of Oscillating Airfoil Dynamic Stall Flow Field", AIAA Paper No. 91-1799, 22nd Fluid Dynamics, Plasmadynamics and Lasers Conference, Honolulu, HI, June 24-27, 1991.

13. Duncan, N.J., Thom, A.S., and Young, A.D., "Mechanics of Fluids", Edward Arnold Pub. Ltd., 1972.

14. Van Dyke, M., "An Album of Fluid Motion", Parabolic Press, 1982.

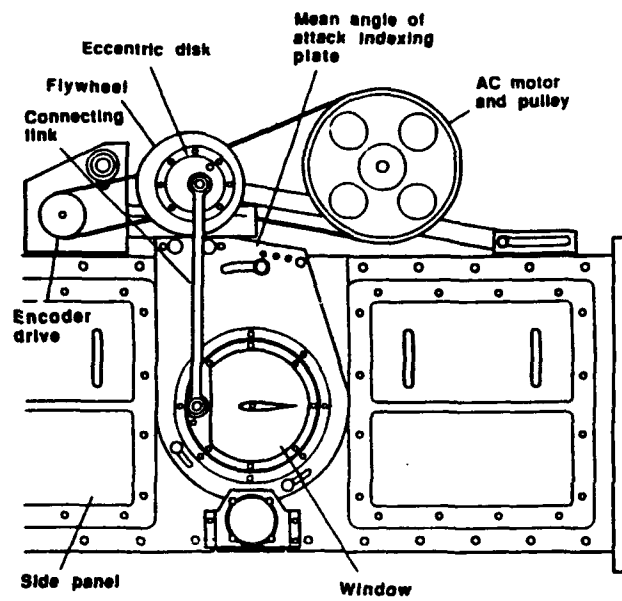15. Goldstein, R.J., "Fluid Mechanics Measurements", Hemisphere Publishing Co, 1983.

Fig. 1. Schematic of the Compressible Dynamic Stall Facility Test Section.
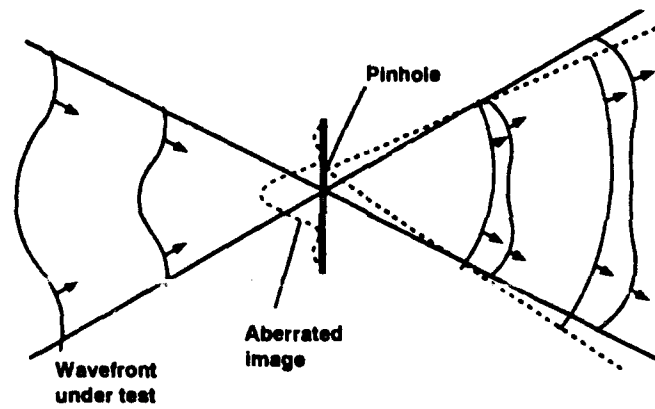

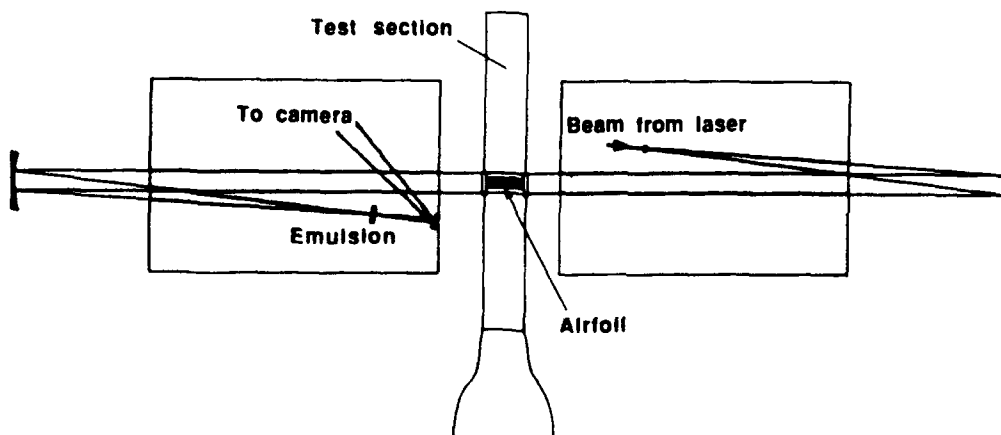Fig. 2. Schematic of the Principle of Point-Diffraction Interferometry.

Fig. 3. Schematic of the Layout of Optics for Point-Diffraction Interferometry.

Figure 4. Point-Diffraction Interferogram of Oscillating Airfoil, $\alpha = 10.0°$, k= 0.075, $M_\infty = 0.33$.

Figure 5. Point-Diffraction Interferogram of Oscillating Airfoil, $\alpha = 13.6°$, k = 0.075, $M_\infty = 0.33$

Figure 6. Point-Diffraction Interferogram Showing Laminar Separation Bubble at $M_\infty = 0.33$, k = 0.075, $\alpha = 9.0°$
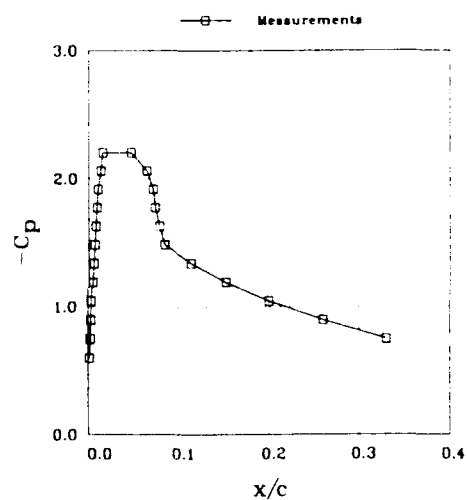
Figure 7. Instantaneous Pressure Distribution Determined From Interferogram at $M_\infty = 0.33$, k = 0.075, $\alpha = 9.0°$.

Figure 8. Point-Diffraction Interferogram Showing Opening of Laminar Separation Bubble at $M_\infty = 0.33$, k = 0.075, $\alpha = 12.4°$.

Figure 9. Point-Diffraction Inteferogram Showing Initial Phase of Dynamic Stall Vortex at $M_\infty = 0.33$, k=0.075, $\alpha = 13.07°$
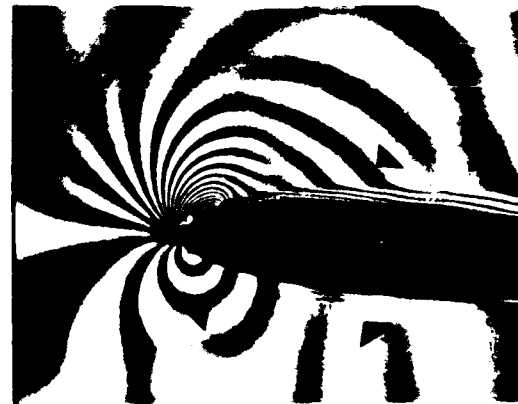
Figure 10. Point-Diffraction Interferograms Showing Effect of Frequency on Dynamic Stall Development at Four Angles of Attack. $M_\infty = 0.30$.

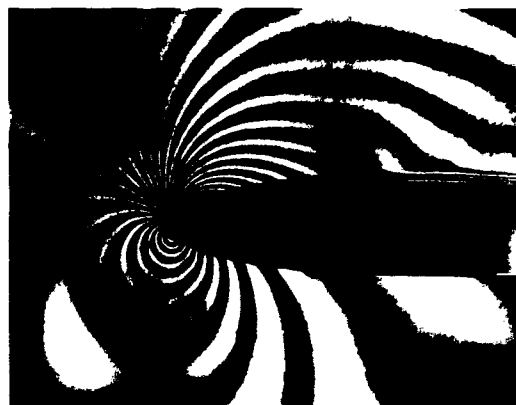$\alpha = 8°$

$\alpha = 10°$

$\alpha = 12°$

$\alpha = 14°$

k = .05

k = .075

Figure 10(continued). Point Diffraction Interferograms Showing Effect of Frequency on Dynamic Stall Development at Four Angles of Attack. $M_\infty = 0.30$.

α = 8°

α = 10°

α = 12°
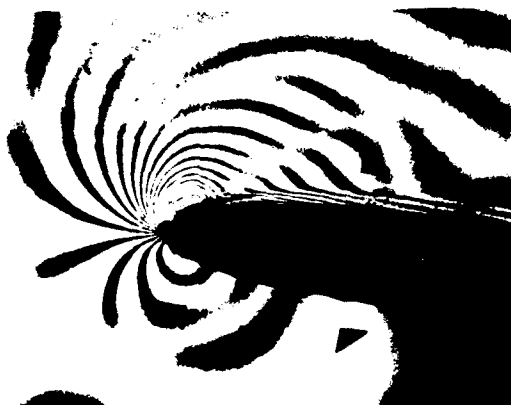
α = 14°

k = .10

Figure 10(concluded). Point-Diffraction Interferograms Showing Effect of Frequency on Dynamic Stall Development at Four Angles of Attack. $M_\infty = 0.30$.

$\alpha = 6°$

$\alpha = 8°$

$\alpha = 10°$
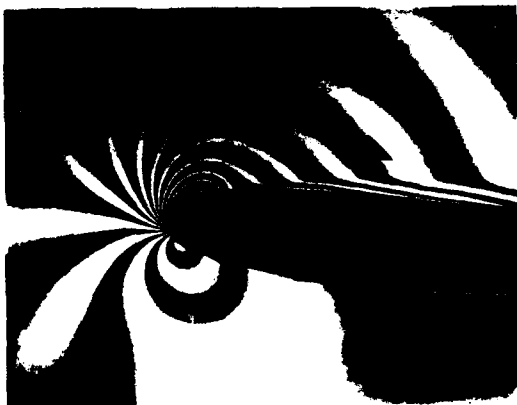
$\alpha = 12°$

M = .28

M = .30

Figure 11. Point-Diffraction Interferograms Showing Effect of Mach Number on Dynamic
Stall Development at Four Angles of Attack. at k = 0.05.

12

$\alpha = 6°$
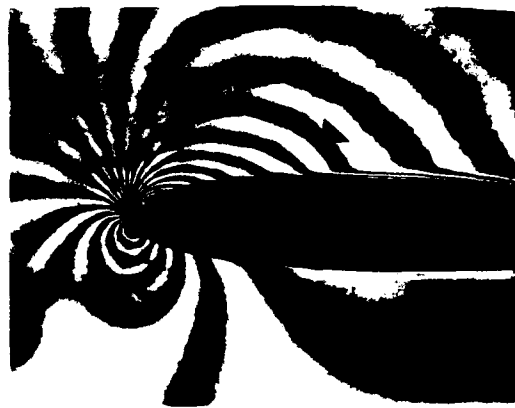
$\alpha = 8°$
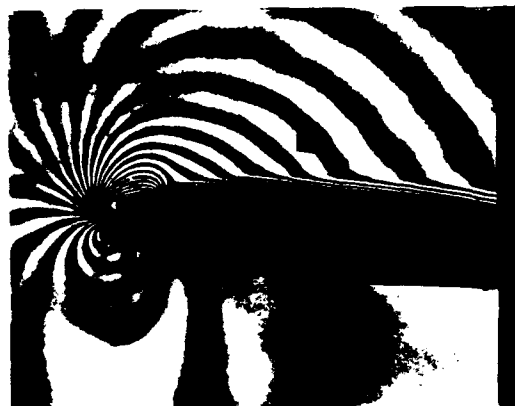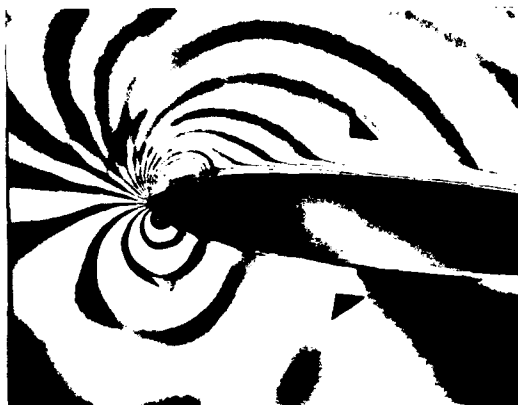
$\alpha = 10°$

$\alpha = 12°$

M = .33

M = .38

Figure 11(continued). Point-Diffraction Interferograms Showing Effect of Mach Number on Dynamic Stall Development at Four Angles of Attack, at k = 0.05.

13

$\alpha = 6°$

$\alpha = 8°$

$\alpha = 10°$

$\alpha = 12°$

M = .42

M = .47

Figure 11(concluded). Point-Diffraction Interferograms Showing Effect of Mach Number on Dynamic Stall Development at Four Angles of Attack, at k = 0.05.
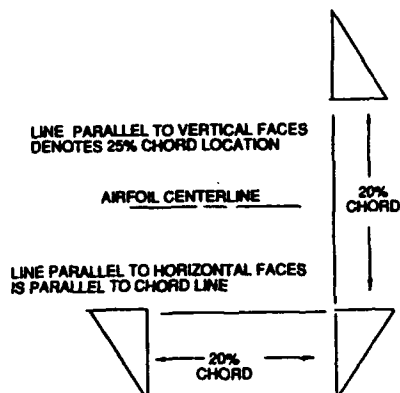
Figure 12. Diagram of Registration Markers placed on CDSF Tunnel Window.
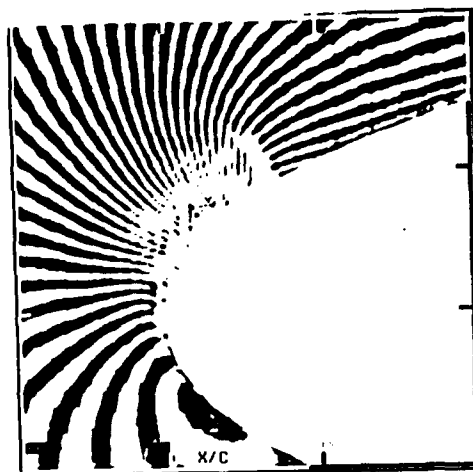
Figure 13. Enlarged Image of Leading Edge Selected From Interferogram(After Digital Enhancement).
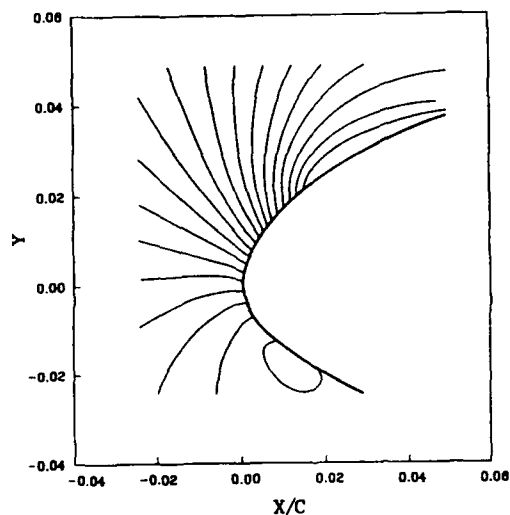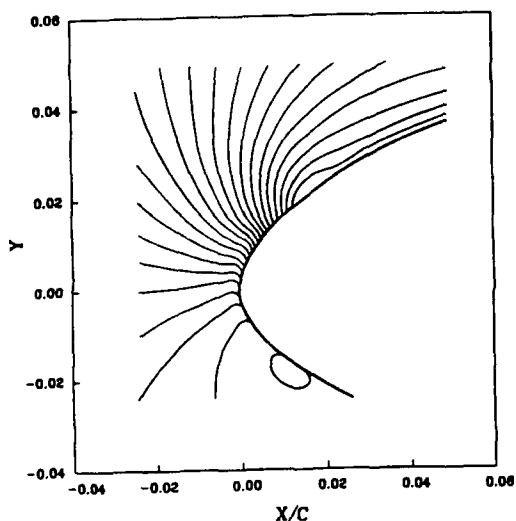
Figure 14. Fringe Contours Near the Leading Edge of an NACA 0012 Airfoil at $M_\infty = 0.33$, $\alpha = 8.0°$, (a) $k = 0.0$; (b) $k = 0.10$.
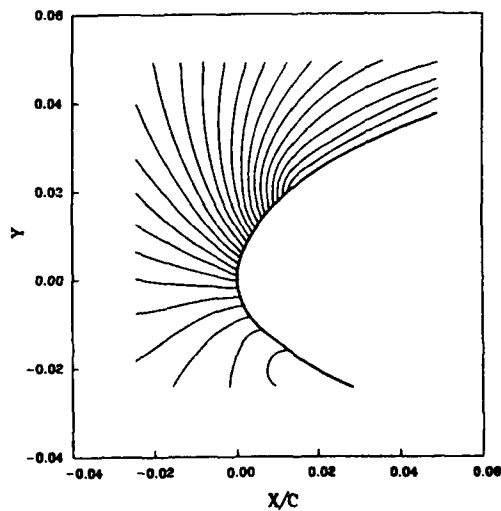
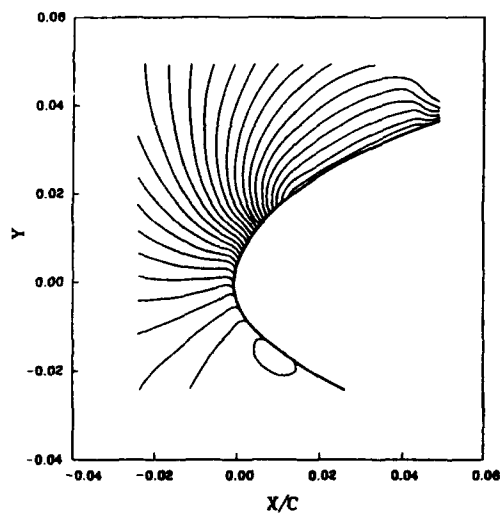Figure 15. Fringe Contours Near the Leading Edge of an NACA 0012 Airfoil at $M_\infty = 0.33$, $\alpha = 10.0°$, (a) $k = 0.0$; (b) $k = 0.10$.
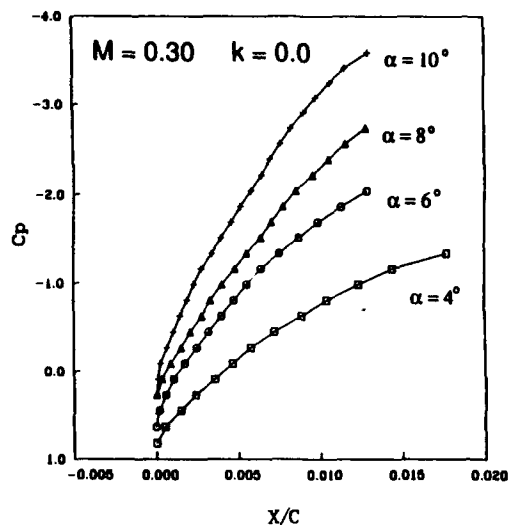
15

Figure 16. Pressure Distributions for Several Angles of Attack for NACA 0012 Airfoil in Steady Flow as Determined From PDI Interferograms, $M_\infty = 0.30$, k = 0.0.
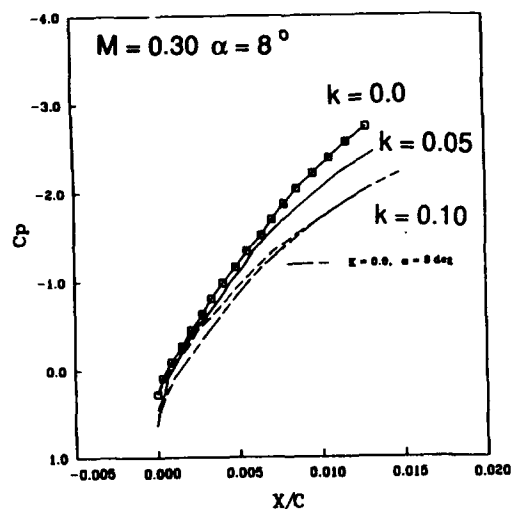

Figure 17. Pressure Distributions for Several Reduced Frequencies for NACA 0012 Airfoil as Determined From PDI Interferograms, $M_\infty = 0.30$, $\alpha = 8.0^o$.
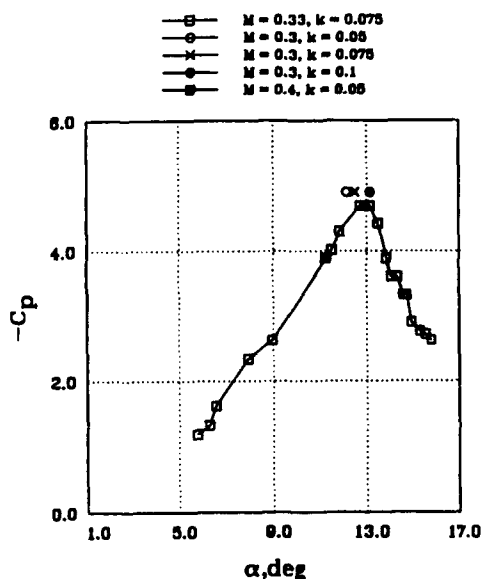

Figure 18. Minimum Cp as Function of Angle of Attack at Various Mach Numbers, as Determined From PDI Interferograms.